ASTRONOMY
AND
ASTROPHYSICS

ESO 138 G1: a high excitation Seyfert 2 nucleus in a low luminosity early-type galaxy*

D. Alloin[1], E. Bica[2], C. Bonatto[2], and P. Prugniel[3]

[1] URA 173 CNRS, Observatoire de Paris/Meudon, F-92195 Meudon, France
[2] Departimento de Fisica, UFRGS, Porto Alegre, RS-91500 Brazil
[3] Observatoire de Haute Provence, CNRS, F-04870 St Michel l'Observatoire, France

Abstract. We analyze in detail the spectral properties of the active nucleus ESO 138 G1. We find that this nucleus lies at the heart of a low luminosity elliptical, making it a particularly interesting and rare object. We have been able to model the continuous energy distribution over the wavelength range $\lambda\lambda 3400$–9700, by an old stellar population which has reached at most a solar metallicity and contributes 60% of the flux at $\lambda 5870$, together with a younger population at age less than 1 Gyr. After subtraction of the stellar population contribution, we have obtained the pure emission line spectrum from the active nucleus. It displays a wide range of ionization species, which for iron in particular goes from [Fe II] up to [Fe XI] and possibly [Fe XIV]. The main line ratios observed in ESO 138 G1 lead us to classify this active nucleus as a Seyfert 2 nucleus. A detailed analysis of the emission lines reveals that there exists in this object, a stratification of the emitting gas clouds according to their density and dominant ionization stage. The width of the lines is observed to correlate with their critical density. The N/O abundance ratio in the gas is about three times larger than the solar value; this result is consistent with the emitting gas being intrinsic material at the center of an elliptical galaxy. Compared to the other two active nuclei which are known so far to exhibit such a high excitation line spectrum, IIIZw77 and Tol 0109–383, ESO 138 G1 builds up a sequence of spectral properties which can be understood if the mean electron density and the excitation of the gas clouds decrease from IIIZw77 to ESO 138 G1. As the spectral properties of the nucleus in IIIZw77 appear to bridge it with radiogalaxies, we might be seeing, along the sequence, ESO 138 G1→Tol 0109–383→IIIZw77→radiogalaxies, an increasing efficiency of matter accretion in systems with increasing mass, from dwarf to giant galaxies.

Key words: galaxies: active – galaxies: Seyfert – galaxies: dwarf elliptical – galaxies: abundance – lines: profile – galaxies: stellar content of

1. Introduction

The galaxy ESO 138 G1 was classified in the ESO Catalogue (Lauberts 1982) as an E/S0. In the course of a redshift survey, Fairall (1988) derived its radial velocity, $V_R = 2740$ km s^{-1} and pointed out its Seyfert 2 nature. He also concluded that ESO 138 G1 belongs to a small group of galaxies, projected in front of the Centaurus–Pavo supercluster.

The ESO photometric Catalogue (Lauberts & Valentijn 1989) provides: $\alpha(1950) = 16\text{h } 47.0 \text{ min}$, $\delta(1950) = -59°09.1'$, $l = 329°.6$ and $b = -9°.44$, quite a low Galactic latitude object. The apparent total blue and red magnitudes are respectively $B_T = 14.35$ and $R_T = 13.02$. The galaxy size is 79'' at the $B = 26$ isophotal level while the axial ratios a/b at various isophotal levels range from 1.48 to 2.00. Adopting a revisited distance of 22 Mpc for this object (Prugniel et al. 1992), we find its absolute blue magnitude to be -18.5 suggesting that we are dealing with a galaxy at the transition between dwarf and standard ellipticals.

While most radiogalaxies appear to be related to giant elliptical galaxies, a low luminosity early type galaxy hosting an active nucleus is a rather rare phenomenon (Adams 1977). In the current paper, we carry out a spectroscopic and image analysis of ESO 138 G1, (i) to study per se this recently discovered Seyfert 2 nucleus and (ii) to test the promising occurrence of an active nucleus at the heart of a low luminosity elliptical or S0 galaxy.

We discuss in Sect. 2 the 2-dimensional photometric properties of the galaxy. In Sect. 3 we elaborate on its central underlying stellar content in order to extract the pure nuclear emission spectrum which is extensively discussed in Sect. 4. Then, ESO 138 G1 is compared to other types of AGN and in particular to the other two high excitation Seyfert nuclei so far known in detail, in Sect. 5.

2. 2-dimensional photometric analysis of ESO 138 G1

The 2-dimensional photometric analysis has been performed using the ESO Catalogue blue image (Lauberts & Valentijn 1989), together with aperture photometry (Prugniel et al. 1992). The large scale environment of ESO 138 G1 is crowded with foreground stars as well as with two bright galaxies, NGC 6215

Table 1. Galaxies in the large-scale environment of ESO 138 G1

Galaxy	α(1950)	δ(1950)	cz (km s^{-1})	B_T	d (")	D (Mpc)
ESO 137 G38	16 36 29	$-60°$ 17 48	2100	12.7	105	630
ESO 137 G45	16 46 36	$-60°$ 43 24	3351	13.3	94	564
ESO 138 G4	16 48 30	$-58°$ 51 54	2894	14.2	21	126
ESO 138 G5	16 49 35	$-58°$ 41 48	2839	12.8	34	204

($H_0 = 100$ km s^{-1} Mpc^{-1}).

Table 2. Parameters for the fit of an $r^{1/4}$ law to ESO 138 G1 aperture photometry

P.A. at minimum b/a	$0.65°$
Asymptotic magnitude	14.13
Mean surface brightness	21.39 mag arcsec^{-2}
Effective radius	11.3 arcsec
Corrected B_T[a]	13.18
Corrected surface brightness[a]	20.44 mag arcsec^{-2}

[a] Galactic absorption $A_B = 0.90$.

($B_T = 11.6$) and NGC 6221 ($B_T = 10.9$) lying respectively 15' and 11' away. ESO 138 G1 is possibly a member of a small group of galaxies comprising the objects listed in Table 1.

Because of its low Galactic latitude, ESO 138 G1 is subject to a rather large foreground reddening, just at the threshold of applicability of the Burstein and Heiles' prescription (1984). Extrapolation of the latter provides a value $A_B = 0.95 \pm 0.2$, whilst a lower limit estimated from the nearest available galaxies is $A_B = 0.87$. In the following we adopt $A_B = 0.90$, implying $E_G(B-V) = 0.22$ for the foreground Galactic colour excess.

From the aperture photometry and the ESO photographic aperture magnitudes (Laubert & Valentijn 1989), the fit of an $r^{1/4}$ curve of growth provides the parameters in Table 2. Together with its absolute blue magnitude these parameters make ESO 138 G1 fulfil the criteria for a low-luminosity early type galaxy, LLE (Prugniel et al. 1992).

The surface photometry performed from the ESO blue image leads to the photometric profile presented in Fig. 1, together with its axis ratio and position angle profiles. The profile shape is between an $r^{1/4}$ law and an exponential profile, thus not unusual for an LLE. The isophote map is shown in Fig. 2. The nearby object ($B_T = 17.9$) at 5" SE to the nucleus has been found to be a foreground star, from its spectral analysis (P. Fouqué, private communication 1992).

We conclude from this photometric analysis that ESO 138 G1 is a low luminosity elliptical/S0 galaxy. The presence of an active nucleus in this system is therefore particularly unusual and exciting and we now turn to the study of the nucler spectrum.

3. The underlying stellar population in ESO 138 G1

Spectroscopic observations were collected on the 21st of May 1990, at the ESO 1.52 m telescope (La Silla) with a Boller and Chivens spectrograph. Two 20 min exposures were obtained with
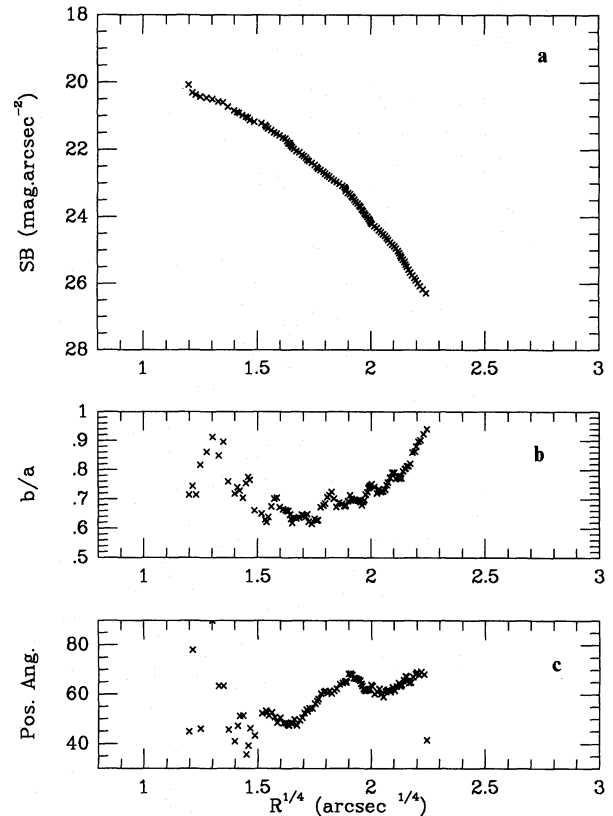

Fig. 1a–c. Photometric profile of the galaxy ESO 138 G1, from aperture photometry and ESO blue image surface photometry. **a** The surface brightness profile (mag arsec^{-2}), **b** the axis ratio and **c** the position angle

the high resolution RCA CCD, 660×1024 pxl (ESO #13). A 450 Å mm^{-1} grating was used in the first order, with an entrance slit width of 1.5". Such a configuration allows one to span, in a single exposure, the $\lambda\lambda 3400$–10 000 range with an 18 Å spectral resolution.

A standard CCD reduction was carried out with the IHAP package at ESO (Garching). As the observations were obtained with a long slit along the EW direction, we have extracted 8 pxl rows for the galaxy nucleus, corresponding to 5.8". (see Fig. 2). Thus, the spatial coverage of the galaxy nuclear spectrum that we discuss in the following is 0.4×1.5 kpc.

We show in Fig. 3 the average of the two ESO 138 G1 spectra, corrected for the Galactic foreground reddening $E_G(B-V) = 0.22$. Notice the outstanding [O III] $\lambda 4959$, 5007 lines, as well
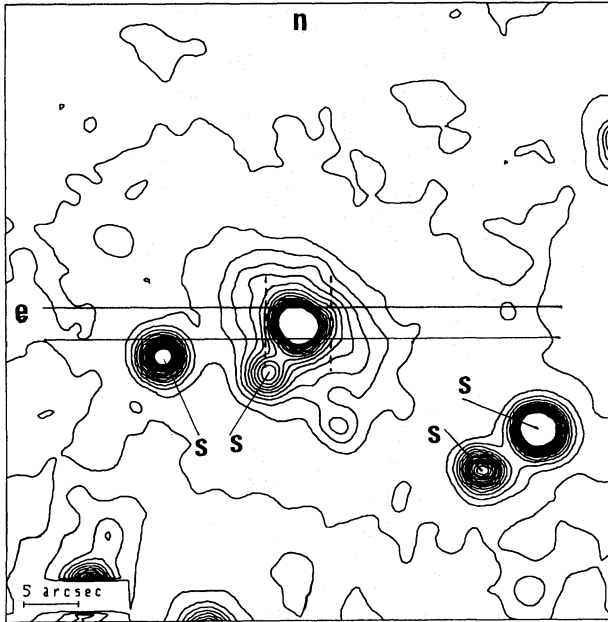
Fig. 2. Isophote map, in the blue, of ESO 138 G1. The objects marked S appear to be foreground stars. The slit used for our spectroscopic observations has been displayed, as well as the limits of the extraction window. With a seeing value on this plate of 2.1 arcsec (FWHM of stars), the nucleus of ESO 138 G1 is not resolved. The scale, at D = 22 Mpc is 1 arcsec = 0.1 kpc

excitation line spectrum of ESO 138 G1 indicates that a powerful ionizing source is present in this object, either from hot stars or from a nonstellar component. Yet, on one hand, this source does not manifest itself on the observed continuum which drops significantly in the blue. And, on the other hand, the large intrinsic reddening found in ESO 138 G1 from Balmer line ratios suggests that the ionizing source might be embedded within dusty absorbing material. Such a characteristic is a distinctive property of Seyfert 2 nuclei.

Therefore, we have sticked to the assumption that the observed continuum is mainly related to the nuclear stellar population and it is the *continuum distribution* that we have attempted to represent by a stellar population model built up through testing different galaxy population templates from Bica (1988). We found that a combination of the blue templates S6 and S7 with proportions 0.7 and 0.3 respectively, reproduces best the observed continuum without the need for an additional nonstellar component. This population model, together with the residual population-subtracted spectrum, are presented in Fig. 4. In terms of flux fractions at $\lambda 5870$ Å, the characteristics of the population model are: 56% for the component with an age ≥ 10 Gyr, 6% for 1 Gyr $\leq$ age ≤ 10 Gyr, 23% for 50 Myr $\leq$ age ≤ 1 Gyr, and 15% for a young component with an age ≤ 50 Myr. Thus, the old bulge-type population appears to be dominant in the observed aperture, together with a noticeable contribution from recently formed stars. The maximum metallicity in the model is found to be solar, consistent with the fact that this nucleus is hosted by a low luminosity galaxy.

as the He II $\lambda 4686$ and [Ne V] $\lambda 3425$ lines characteristic of a highly excited Seyfert 2 nucleus. In order to emphasize its continuum distribution and its lines of moderate to weak strength, the nuclear spectrum has been displayed in Fig. 4 on an expanded intensity scale. The continuum appears to be quite blue with maximum emission at about $\lambda 4600$. The emission line spectrum is so strong that only a few stellar absorption features from the underlying population can be recognized, such as the G band, Mg I, TiO bands and the Ca II IR triplet.

The spectra were obtained at a mean hour angle of 45 min, which makes the atmospheric differential refraction occurring along a 25° position angle. The distances between the visible image $\lambda 4500$ and the blue $\lambda 3500$ or red $\lambda 9000$ images are of plus and minus 0.5″. With the EW slit orientation, a 1.5″ slit width and a 2″ seeing, this leads to a 15% uncertainty on the spectral energy distribution of ESO 138 G1, between its two extreme blue and red ends. Although it is theoretically possible to correct back for the atmospheric differential refraction effect, consideration of seeing losses together with additional slight uncertainties in slit centering and guiding makes such a correction rather vain. We simply retain a global 15% uncertainty on the spectral energy distribution, over the considered range.

The mixture of the absorption stellar spectrum with the emission nuclear spectrum makes information about the pure stellar absorption features too uncertain and scarce for their valuable use in the derivation of the underlying stellar population. Hence, we can only rely on the continuous energy distribution. And indeed, as the continuum decreases bluewards of $\lambda 4600$, we infer that its main contribution is from the underlying stellar population. This may not be fully correct however. The high

4. The pure emission spectrum in ESO 138 G1

4.1. Spectral characteristics of the emission

The population-subtracted spectrum displays a rich variety of emission lines, in particular of Fe lines up to [Fe XI] and possibly [Fe XIV]. Line intensities have been measured through a gaussian fitting which allows a proper separation of blended features. The gaussian fitting routine is illustrated in Fig. 5 for the [O I] $\lambda 6363$ and [Fe X] $\lambda 6374$ lines. We also provide in Fig. 6 part of the pure emission spectrum over the $\lambda\lambda 5200$–6200 range, where one can see the strong $\lambda 5277$, 5731 and 6087 [Fe VII] lines, the $\lambda 5424$, 5426 [Fe VI] blend, the $\lambda 5303$ [Fe XIV] and $\lambda 5309$ [Ca V] blend and the $\lambda 5527$ [Fe II] as well as the $\lambda 5876$ He I lines. A residue of the Galactic Na I absorption is also visible, in relation with the large intervening reddening towards ESO 138 G1.

The line intensities, relative to $I(H\beta) = 100$, of the pure emission spectrum are given in Table 3. We provide as well the FWHM (km s^{-1}) of the various lines. The observed Balmer decrement $I(H\alpha)/I(H\beta) = 4.25$ suggests an additional intrinsic colour excess $E_i(B - V) = 0.32$. Besides, the line ratios [O II]$\lambda 7319 + 7331$/[O II]$\lambda 3726 + 3729$ and [S II]$\lambda 4068 + 4076$/[S II]$\lambda 6717 + 6731$ can be used to derive the reddening (Allen 1979). In the case of ESO 138 G1, they indicate an internal colour excess $E_i(B - V) = 0.43$. These line ratios, however, probe the reddening in a region of a narrower density range (Ne $\sim 2 \times 10^3$ cm^{-3}) than the Balmer line ratio Hα/Hβ and are known to lead to an overestimate of the reddening (Mihalszki & Ferland 1983). Therefore, we have adopted in the following, the value $E_i(B - V) = 0.32$ for the intrinsic reddening in ESO 138 G1, which after being taken into account, leads to the corrected
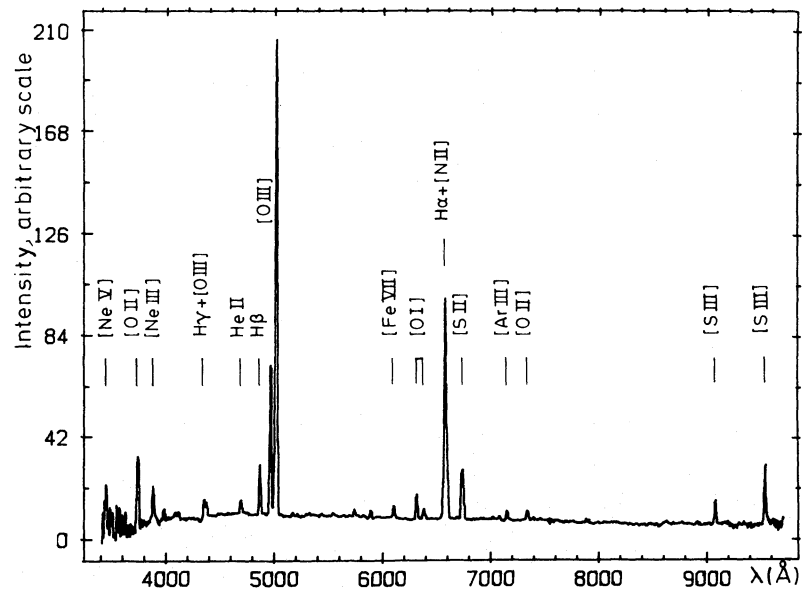
Fig. 3. Galactic reddening corrected [$E(B-V)=0.22$] and restframe spectrum of ESO 138 G1. Notice the wealth of high excitation lines. A negligible contamination ($<5\%$) from the second order spectrum appears at $\lambda>9500$ Å
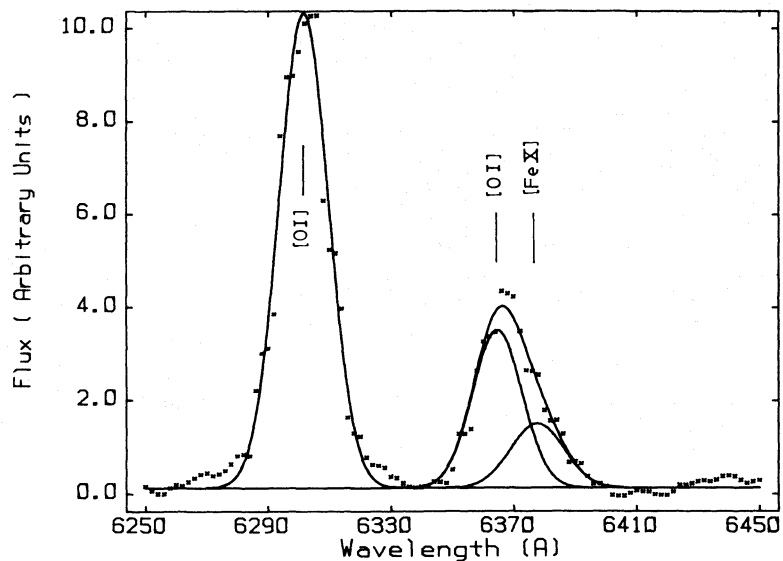

Fig. 4a. Galactic reddening corrected [$E(B-V)=0.22$] and restframe spectrum of ESO 138 G1 on an expanded scale. The trace of an absorption feature, from the underlying stellar population, becomes apparent at the G band, Mg I lines, TiO bands and Ca II IR triplet. Also shown is the stellar population template which best fits the continuum energy distribution of ESO 138 G1 (shifted in flux for a purpose of legibility)

Fig. 5. Illustration of the gaussian fitting procedure. The [O I]$\lambda6300$ and [O I]$\lambda6363$ lines are constrained to have the same width at half maximum and their intensity to be in the theoretical ratio of 3. Then the [Fe X] line can then be properly sorted out from the

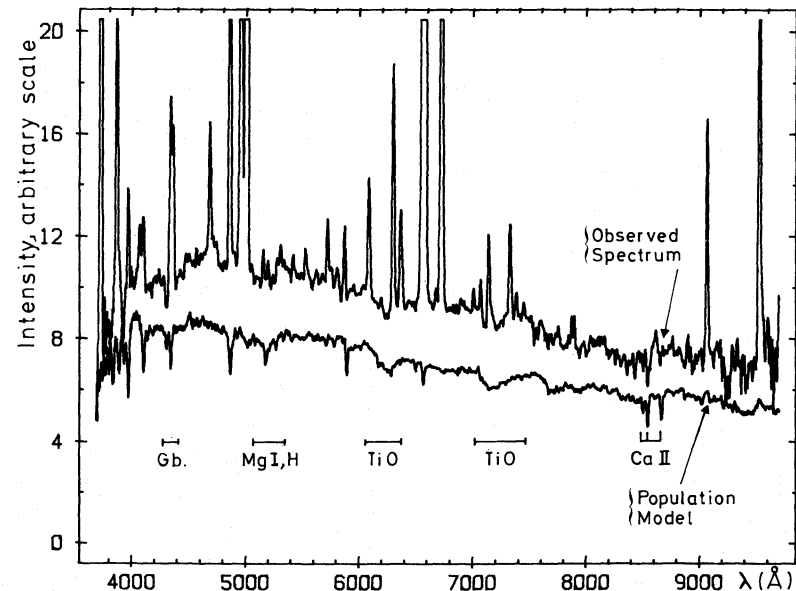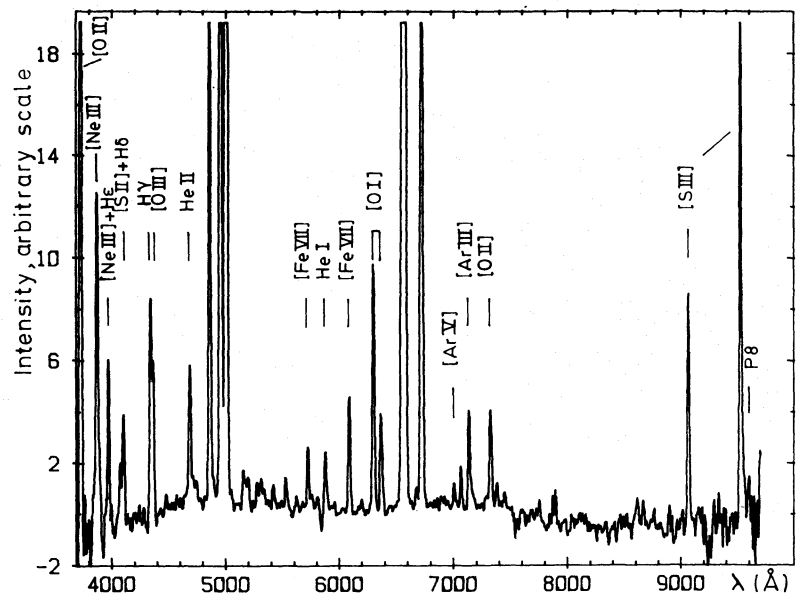**Fig. 4b.** The pure nuclear emission spectrum from the active nucleus in ESO 138 G1. Many weak, high excitation lines show up after subtraction of the stellar population
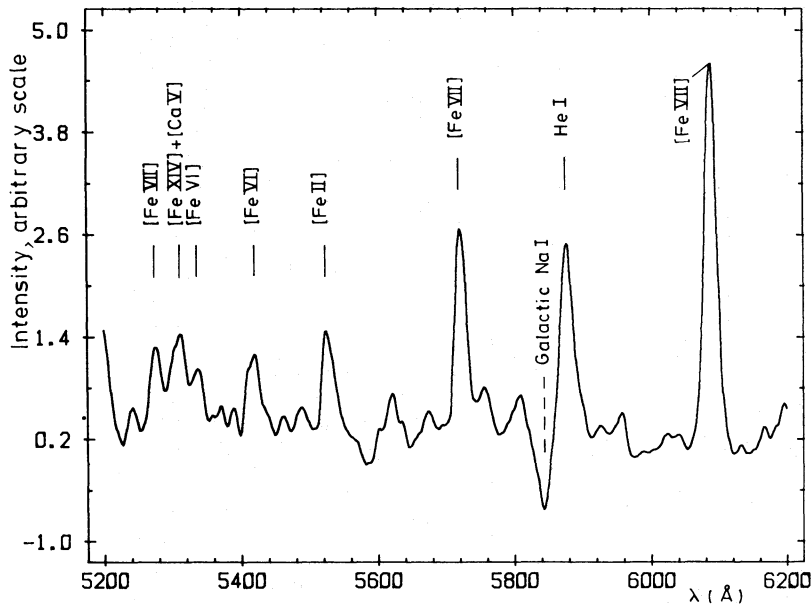
Fig. 6. Enlargement of the emission spectrum in the $\lambda\lambda 5200$–6200 range. One can see the prominent [Fe VII] lines, as well as other faint, high excitation lines. The Galactic Na I line appears in absorption at an unusual wavelength, because it has been improperly shifted back to the galaxy restframe (2740 km^{-1})
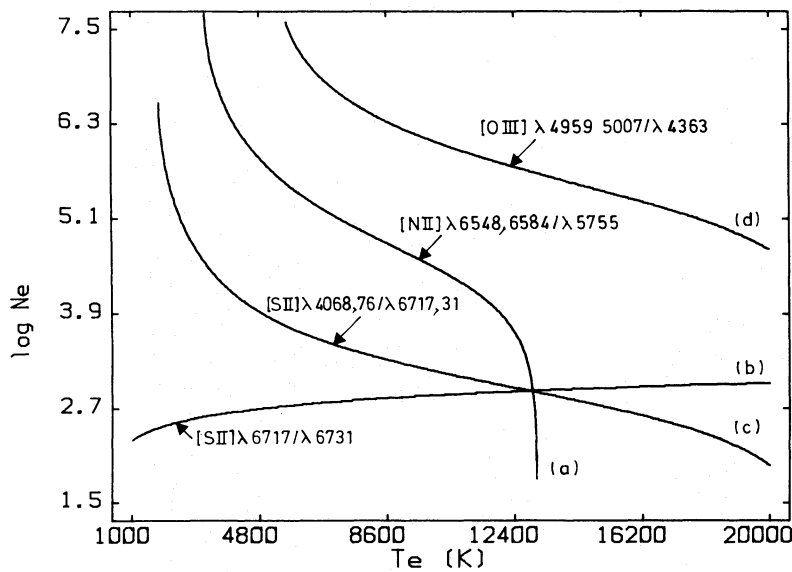

Fig. 7. The theoretical relationship for line intensity ratios have been plotted in the log N_e versus T_e plane. The line ratios corrected for internal reddening in ESO 138 G1 have been used. The curves are labelled as follows: (a) [N II]$\lambda\lambda 6548$, 6584/[N II]$\lambda 5755 = 47.6$; (b) [S II]$\lambda 6717$/[S II]$\lambda 6731 = 0.98$; (c) [S II]$\lambda\lambda 4068$, 4076/[S II]$\lambda\lambda 6716$, $6731 = 0.11$; (d) [O III]$\lambda\lambda 4959$, 5007/[O III]$\lambda 4363 = 34.2$. The curves (a), (b) and (c) which correspond to singly-ionized elements intersect around a same point and define the couple of parameters $N_e = 830 \pm 10$ cm^{-3}, $T_e = 12900 \pm 60$ K

line intensities given in the last column of Table 3. Still, one should bear in mind that $E_i(B-V)$ could only be estimated in a crude way, and that this additional intrinsic reddening affects specifically the emitting clouds.

4.2. Physical conditions of the gas producing the emission spectrum

We can use standard line ratios to derive both the electron density N_e and the electron temperature T_e in the emitting regions. Useful line ratios are [N II]$\lambda 6548 + 6584$/[N II]$\lambda 5755$, [S II]$\lambda 6717$/[S II]$\lambda 6731$, [S II]$\lambda 4068 + 4076$/[S II]$\lambda 6717 + 6731$ and [O III]$\lambda 4959 + 5007$/[O III]$\lambda 4363$. The corresponding equations relating line intensity ratios to T_e and N_e are from McCall (1984).

Using the line ratios observed for ESO 138 G1, we have displayed the behaviour of these equations in the $\{\log N_e, T_e\}$ plane (Fig. 7). The three curves corresponding to elements ionized one-time, O$^+$, N$^+$ and S$^+$ intersect around one point which defines the physical conditions in this zone: $N_e = 830 \pm 50$ cm^{-3} and $T_e = 12900 \pm 100$ K. For twice-ionized elements, only the [O III] line ratio can be used and therefore, we can only estimate N_e within a temperature interval. Let us consider the plausible range 10^4 K $\leq T_e \leq 2\,10^4$ K: the observed [O III] line ratio being 34.2, implies for the O^{++} zone an electron density in the range $5\,10^4$ cm$^{-3} \leq N_e \leq 1.2\,10^6$ cm^{-3}, considerably higher than that found in the O$^+$, N$^+$, S$^+$ zone. This result suggests that an ionization and density structure exists in the emission line region of ESO 138 G1, with the elements at higher ionization levels having a tendency to lie closer to the central source, in

Table 3. Emission line parameters in the pure emission spectrum of ESO 138 G1

Line identification	FWHM (km s^{-1})	Intensity corrected for $E_G(B-V)=0.22$	Intensity corrected for $E_G(B-V)=0.22$ and $E_i(B-V)=0.32$
[Ne v]$\lambda 3425$[a]	2000:	122 ± 10	176 ± 10
[Fe vii]$\lambda 3587$	700:	16.6 ± 3	23 ± 3
[O ii]$\lambda 3726, 29$	1820*	174 ± 5	235 ± 5
[Fe vii]$\lambda 3759 +$ O iii$\lambda 3760$	720:	8.5 ± 2	12 ± 2
H9$\lambda 3835$	1070	10.8 ± 2	14.0 ± 2
[Fe vi]$\lambda 3847 +$ [Fe v]$\lambda 3840, 3852$	710*	7.5 ± 2	9.5 ± 2
[Ne iii]$\lambda 3870$	1580	78.4 ± 3	100 ± 3
He i + H8$\lambda 3888$	730	5.5 ± 1	6.8 ± 1
[Fe v]$\lambda 3896$	1430*	10.5 ± 3	13.3 ± 3
[Ne iii]$\lambda 3967$	1560	28.5 ± 3	35.6 ± 4
Hε + He ii$\lambda 3970$	900	5.9 ± 2	7.4 ± 2
[S ii]$\lambda 4068, 76$	950*	8.5 ± 1	10.4 ± 1
H$\delta\lambda 4101$	1490	23.7 ± 2	28.7 ± 2
[Fe iv]$\lambda 4206$	1180	3.5 ± 1	4.2 ± 1
[Fe v]$\lambda 4227$	750	2.3 ± 1	2.8 ± 1
[Fe ii]$\lambda 4244$, m.21	650	3.1 ± 1	3.6 ± 1
Fe ii$\lambda 4278$, m.32 + [Fe ii]$\lambda 4277$, m.21	1530*	4.9 ± 2	5.7 ± 2
H$\gamma\lambda 4340$	1390	48.3 ± 2	55.2 ± 2
[O iii]$\lambda 4363$	1240	30 ± 2	34 ± 2
He i$\lambda 4471$	1400	4.0 ± 1	4.4 ± 1
He ii$\lambda 4686$	1350	29.3 ± 2	30.6 ± 2
He i + [Ne iv]$\lambda 4714$[b]	850*	3.5 ± 1	3.6 ± 1
[Ar iv]$\lambda 4740$	1760	6.5 ± 1	6.5 ± 1
H$\beta\lambda 4861$	1130	100 ± 3	100 ± 3
[Fe vii]$\lambda 4893$	960	3.5 ± 1	3.5 ± 1
[O iii]$\lambda 4959$	1110	300 ± 9	293 ± 9
[O iii]$\lambda 5007$	1100	900 ± 25	871 ± 25
He i$\lambda 5048$	1410	5.6 ± 1	5.4 ± 1
[Fe vi]$\lambda 5146 +$ [Fe vii]$\lambda 5159$	1110*	7.5 ± 1	7.2 ± 1
[Fe vi]$\lambda 5176$	920	4.0 ± 1	3.7 ± 1
[Ar iii]$\lambda 5192$	780	3.8 ± 1	3.5 ± 1
[N i]$\lambda 5198, 5200$	1030*	4.7 ± 1	4.3 ± 1
[Fe vii]$\lambda 5277$	1080	5.4 ± 1	4.9 ± 1
[Fe xiv]$\lambda 5303 +$ [Ca v]$\lambda 5309$	1480*	8.2 ± 1	7.4 ± 1
[Fe vi]$\lambda 5335$	1160	4.0 ± 1	3.6 ± 1
[Fe vi]$\lambda 5424, 26$	1450*	6.6 ± 1	5.8 ± 1
[Fe vi]$\lambda 5485$	1040	2.1 ± 0.6	1.8 ± 0.6
[Fe ii]$\lambda 5527$, m.17	1190	7.3 ± 1	6.3 ± 1
[Fe vi]$\lambda 5677$	940	1.6 ± 0.5	1.3 ± 0.5
[Fe vii]$\lambda 5721$	960	12.2 ± 1	10.0 ± 1
[N ii]$\lambda 5755$	730	2.3 ± 1	1.9 ± 1
He i$\lambda 5876$	1180	13.6 ± 2	10.9 ± 2
[Fe vii]$\lambda 6087$	990	24.4 ± 2	18.7 ± 2
(?)$\lambda 6200$	920	3.0 ± 0.8	2.3 ± 0.8
[O i]$\lambda 6300$	900	48.1 ± 2	35.1 ± 2
[O i]$\lambda 6364$	900	16.0 ± 2	11.7 ± 2
[Fe x]$\lambda 6375$	1060	7.5 ± 1	5.5 ± 1
[N ii]$\lambda 6548$	720	32.0 ± 2	22.7 ± 2
Hα	850	425 ± 10	301 ± 10
[N ii]$\lambda 6584$	720	96 ± 3	68 ± 3
He i$\lambda 6678$	790	3.7 ± 1	2.6 ± 1
[S ii]$\lambda 6717$	780	68.8 ± 3	47.6 ± 3
[S ii]$\lambda 6731$	780	70.4 ± 3	48.6 ± 3

Table 3 (continued)

Line identification	FWHM $(\mathrm{km\,s^{-1}})$	Intensity corrected for $E_G(B-V)=0.22$	Intensity corrected for $E_G(B-V)=0.22$ and $E_i(B-V)=0.32$
[Ar v]λ7006	820	4.9 ± 1	3.2 ± 1
He iλ7065	690	7.0 ± 1	4.6 ± 1
[Ar iii]λ7136	740	18.1 ± 2	11.8 ± 2
[?]λ7164	1050	5.2 ± 1	3.4 ± 1
He iλ7281	1280	5.9 ± 1	3.8 ± 1
[O ii]λ7319	720	12.9 ± 1	8.2 ± 1
[O ii]λ7330	720	8.7 ± 1	5.5 ± 1
[Ni ii]λ7378^c	720	4.2 ± 1	2.6 ± 1
[Ar iii]λ7750	790	4.2 ± 1	2.5 ± 1
[Fe xi]λ7892	640	7.2 ± 1	4.3 ± 1
[Fe ii]λ8617, m.13	1250	9.6 ± 1	5.3 ± 1
Fe iiλ8672	770	5.9 ± 1	3.3 ± 1
[Fe ii]λ8892, m. 13	570	5.4 ± 1	2.9 ± 1
P10λ9014	440	2.3 ± 0.6	1.2 ± 0.6
[S iii]λ9069	550	40.6 ± 2	21.7 ± 2
[S iii]λ9532	550	93.7 ± 4	48.4 ± 4
P8λ9554	770	13.1 ± 1	6.8 ± 1
[Fe iii]λ9701 + C iiiλ9697, 9702	620*	18.3 ± 2	9.3 ± 2

Notes to Table 3: ^{a} Measured on the total spectrum including the stellar population contribution; ^{b} Blend with He iλ4713 and [Ne iv]λ4716, 25, 26; ^{c} Blend with several [Ni iii] lines. The error-bars on line-intensities have been estimated according to the noise-level around each line and to the precision of the deblending procedure. All intensities have been normalized to $I(H\beta)=100$.

filaments of higher temperature and larger density. Variations in the FWHM of the forbidden lines, illustrated through the observed relationship (Fig. 8) between the FWHM of a transition line and its critical density (Table 4), complement this conclusion. Similar stratifications have been observed in the narrow line region of NGC 3783 (Pelat et al. 1981), in the LINER NGC 7213 (Filippenko & Halpern 1984) and in the NLR of other AGN (de Robertis & Osterbrock 1986).

The spectrum of ESO 138 G1 is rich in lines from Fe at various ionization stages. It is beyond the scope of the current analysis to fully exploit such an information because, (i) most of these lines are faint and/or blended and would require to be analyzed from a spectrum through a smaller entrance aperture, in order to dim the contribution from the absorption stellar component and with a higher spectral resolution, and (ii) iron is a difficult element to study from the point of view of atomic physics. Only the [Fe vi] and [Fe vii] lines will be considered below to derive some constraints on the physical conditions to be found in the region where they are formed. Using the emissivities predicted by Nussbaumer & Storey (1978), the line ratio [Fe vi] λ5424 + 5427/[Fe vi]λ5335 provides $N_e=10^6$ cm^{-3} for 10^4 K $\leq T_e \leq 2\,10^4$ K, the line ratio [Fe vi]λ5176/[Fe vi]λ5335 gives 10^4 cm$^{-3} \leq N_e \leq 10^5$ cm^{-3}, while the upper limit on [Fe vi]λ5146/[Fe vi]λ5335 is consistent with $N_e \leq 10^6$ cm^{-3} on the same T_e interval. Taking into account the around 30%

uncertainty on such faint lines, we can conclude that N_e is in the range 10^5–10^6 cm^{-3} in the clouds where Fe^{5+} predominates.

If we now turn to the [Fe vii] lines, we have considered the two line ratios studied by Nussbaumer & Storey (1982) and for which we obtained upper limits in ESO 138 G1, [Fe vii]λ3759/ [Fe vii]λ6087 ≤ 0.64 and [Fe vii]λ5159/ [Fe vii]λ6087 ≤ 0.39. The former imposes $T_e < 1.5\,10^4$ K and provides $N_e \leq 10^7$ cm^{-3}
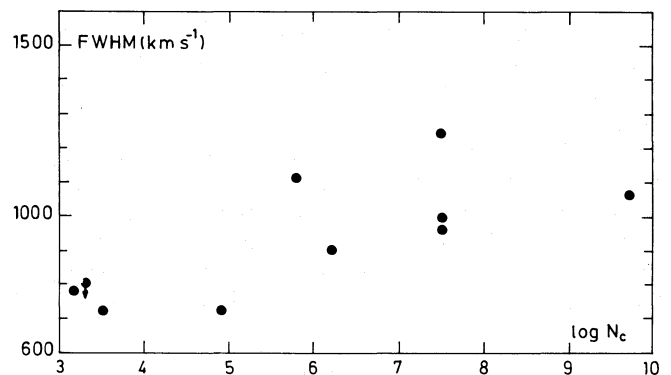

Fig. 8. The observed relationship between the FWHM (km s^{-1}) and the critical electronic density N_c (cm^{-3}) of the transition lines in ESO 138 G1

Table 4. The FWHM (km s^{-1}), ionization potential and critical density N_c(cm^{-3}) of the observed line transitions in ESO 138 G1. The critical density is given for $T_e = 10^4$ K

Transition	FWHM	χ	N_c
[O III]λ4363	1240	35.1	3.3 10^7
[O III]λ5007	1110	35.1	7 10^5
[N I]λ5200	<800	0.0	2 10^3
[Fe VII]λ5721	960	99.1	3.6 10^7
[Fe VII]λ6087	990	99.1	3.6 10^7
[O I]λ6300	900	0.0	1.8 10^6
[Fe X]λ6375	1060	233.6	4.8 10^9
[N II]λ6584	720	14.5	8.7 10^4
[S II]λ6731	780	10.4	1.5 10^3
[O II]λ7319	720	13.6	3.1 10^3

if T_e is set to $1.5\ 10^4$ K; yet, the O IIIλ3760 Bowen line blended with [Fe VII]λ3759, which makes this ratio only an upper limit certainly contributes very little to the blend and we may use the equality value which leads to $T_e = 1.5\ 10^4$ K and $N_e = 10^7$ cm^{-3}. The latter ratio is compatible with such conditions and does not add any new constraint, being an upper limit only.

Therefore, the information we can draw from the [Fe VI] and [Fe VII] lines in ESO 138 G1 is that, in the region where the [Fe VI] lines are emitted, $T_e \leq 1.5\ 10^4$ K and N_e is in the range 10^5–10^6 cm^{-3}, while the [Fe VII] lines may arise from a region at $T_e = 1.5\ 10^4$ K and $N_e = 10^7$ cm^{-3}. This is probably also the zone where the [O III]λ4363 line is formed. This result also argues for the density stratification previously discussed. The [Fe X]λ6374 and [Fe XI]λ7892 line intensities interpreted in the framework of simple photoionization models (Grandi 1978), are consistent with the analysis and the results we have just discussed.

4.3. Abundances in the emitting gas

We have used the code ABELION kindly made available by Stasinska (1990; private communication, 1992) to compute the heavy element abundances in ESO 138 G1.

We obtain then, for the singly-ionized zone:

$$(O^+/H) = 1.74\ 10^{-4},$$

$$(N^+/H) = 3.46\ 10^{-5}.$$

We can derive with relative confidence the ratio N/O = 0.2, and a lower limit only for the O/H abundance, $2\ 10^{-4} <$ O/H.

The striking result is that the N/O ratio in ESO 138 G1 is about 6 times larger than in the Large Magellanic Cloud and about 3 times larger than in the solar vicinity. Such large values of the N/O ratio are common in galaxy nuclei and plea for both a primary and secondary production of N [see e.g. the early discussions by Alloin et al. 1979 and Pagel and Edmunds 1979]. They also indicate that the emitting material in ESO 138 G1 is intrinsic gas rather than recently captured external gas.

6. Comparison of ESO 138 G1 with other types of AGN

Two comparable high excitation active nuclei have been reported on, so far, from their detailed spectrum, IIIZw77 (Osterbrock
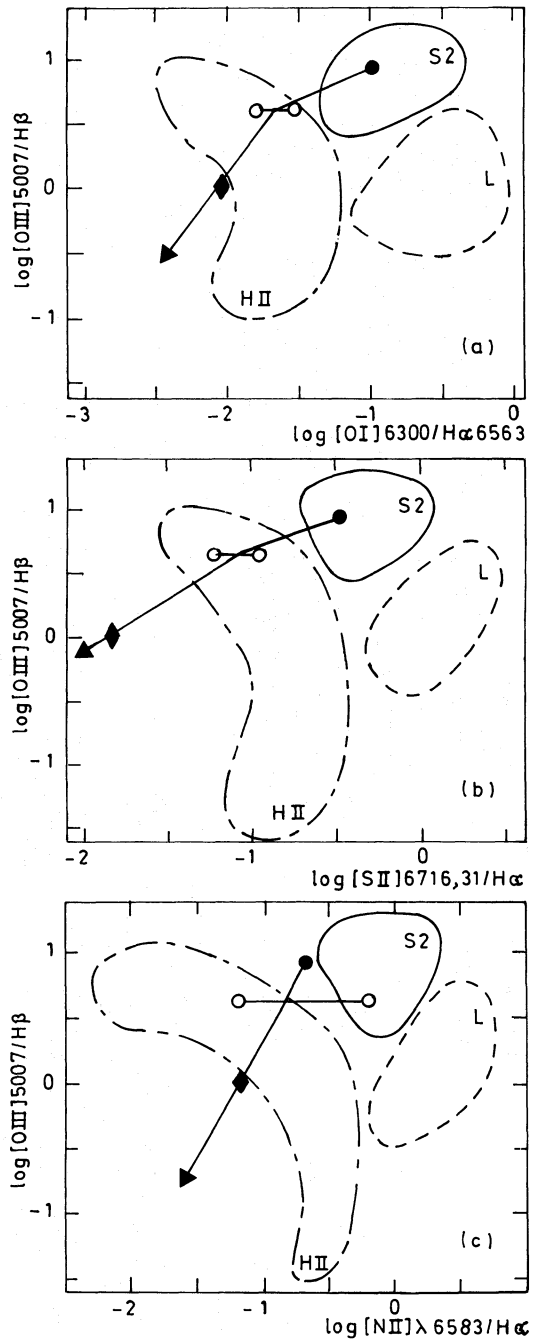

Fig. 9a–c. The position of ESO 138 G1 (black circle), Tol 0109–383 (open circle) and IIIZw77 (black diamond) in three diagnostic diagrams from Veilleux & Osterbrock (1987): **a** the [O III]/Hβ vs. [O I]/Hα plot; **b** the [O III]/Hβ vs. [S II]/Hα plot; **c** the [O III]/Hβ vs. [N II]/Hα plot. The locus of various active objects are shown: Plain curve: Seyfert 2 nuclei, S2; dotted curve: Liners, L; dash-dotted curve: H II region type nuclei, H II. For Tol 0109–383, we have attempted two different interpretations of the Hα, [N II] blend: a very small contribution from [N II], then implying that the Balmer ratio is far from the Case B one, and an [N II] contribution which places Hα/Hβ at the standard value $\sim$3. These diagnostic diagrams are not very sensitive to the intrinsic reddening value adopted for each object. The three high excitation nuclei define a sequence of increasing N_e and excitation, from ESO 138 G1 to IIIZw77. The latter object, devoid of gas clouds with low densities around 10^{-3} cm^{-3}, shows spectral properties which link it to radiogalaxies

Table 5. Comparison of the intrinsic line intensities in three high excitation Seyfert 2 nuclei

	ESO 138 G1[a]	Tol 0109–383[b]	IIIZw77[c]
[Ne v]λ3425	176	136	43
[O ii]λ3726, 3729	235	67	11
[Ne iii]λ3870	100	51	22
[Ne iii]λ3967	36	18	8.6
[S ii]λ4068, 4076	10.5	9	3.7
Hδ λ4101	29	20	21
Hγ λ4340	55	48	43
[O iii]λ4363	34	27	10.5
He iλ4471	4.5	4	
He iiλ4686	30	25	33
H$\beta\lambda$4861	100	100	100
[O iii]λ4959	293	140	37
[O iii]λ5007	871	425	105
[Fe vi]λ5146 + [Fe vii]λ5159	7.2	4.0	2.0
[N i]λ5198, 5200	4.3	3.0	1.1
[Fe xiv] + [Ca v]λ5303	7.4	8.0	4.5
[Fe vii]λ5721	10.0	10.0	4.8
[N ii]λ5755	2.0	2.0	
He iλ5876	11	7:	4.8
[Fe vii]λ6087	19	19	8.3
[O i]λ6300	35	9.0	3.3
[O i]λ6363	12	3.0	1.2
[Fe x]λ6374	5.5	13	6.7
[N ii]λ6548	23		5.8
Hα λ6562	301	} 577	305
[N ii]λ6584	68		20
[S ii]λ6717	48	15	2.0
[S ii]λ6730	49	18	2.2
[Ar iii]λ7136	12	11	1.2
[O ii]λ7319, 7330	14	6	1.5
[O iii]λ4363/4959, 5007	0.029	0.048	0.074
[Ne v]λ3425/[Ne iii]λ3870, 3967	1.30	1.97	1.67
[S ii]λ4068, 4076/λ6717, 6730	0.11	0.27	0.88
[O ii]λ7319, 7330/λ3727, 3729	0.058	0.090	0.136
[O i]λ6300, 6363/[O ii]λ3727, 3729	0.20	0.18	0.40
[O ii]λ3727, 3729/[O iii]λ4959, 5007	0.20	0.12	0.08

[a] Line intensities corrected for $E_i(B-V) = 0.32$ (this paper).
[b] Line intensities corrected for $E_i(B-V) = 0.53$ (Fosbury & Sansom 1983).
[c] Line intensities corrected for $E_i(B-V) = 0.32$ (original values from Osterbrock 1981).

1981) and Tol 0109–383 (Fosbury & Sansom 1983). The former lies in a compact Zwicky galaxy with apparent diameter less than 2″, at a redshift $z = 0.03374$, about 3.7 times further away than ESO 138 G1. The latter is at the centre of a spiral-like galaxy (Smith 1975), with a redshift $z = 0.009$, close to that of ESO 138 G1.

For all three active nuclei, the emission line spectrum is extremely rich in observed species and in multiple ionization stages, for iron in particular. Another common property between the three objects seems to be their rather large intrinsic reddening, as derived from the Balmer line ratios or the [O ii], [N ii] line ratios. Notice however that, in the case of IIIZw77 and Tol 0109–383, this determination is even more uncertain because of the presence of a broad component in the hydrogen line spectrum.

For a comparison at first order between the spectral properties of the three nuclei, we provide in Table 5 the intensities of their main emission lines, corrected for an intrinsic color excess $E_i(B-V)$ of 0.32, 0.53 and 0.32 respectively in ESO 138 G1, Tol 0109–383 and IIIZw77.

Tol 0109–383 and ESO 138 G1 exhibit rather similar spectra although a slightly higher excitation can be noticed in Tol 0109–383: a larger [Ne v] to [Ne iii] line ratio, a larger [Fe x] and fainter [O i], [O ii], [O iii] lines implying that more oxygen is in the form of O^{+3} in this object.

The spectrum of IIIZw77 looks significantly different with more prominent Balmer lines, a larger [O iii]λ4363/[O iii]λ4959, 5007 line ratio and much weaker lines from low ionization species having transitions at low critical densities such as [O ii], [N ii] and [N i]. This fact suggests that IIIZw77 contains gas

clouds with a larger mean density, above 10^3–$10^5\,\mathrm{cm}^{-3}$ and is lacking the gas clouds at $N_e \sim 10^3\,\mathrm{cm}^{-3}$ which generally emit the [O II], [N II] strong lines observed in conventional galaxy nuclei.

Ranking the three nuclei from ESO 138G1 to Tol 0109–383 and then IIIZw77, we observe that the He II/He I, [O I]/[O II] and [O III]/[O II] line ratios increase by a factor around 2, the He II/Hβ and [Ne V]/[Ne III] line ratios remain about the same and finally the [O III]/Hβ and [O II]/Hβ line ratios both drop by a factor between 8 and 20. In the light of the photoionized models described by Stasinska (1984, 1990), these observational facts suggest that the dominant source of spectral changes along this sequence is a variation of the mean electron density.

Let us now compare the spectral properties of the three high excitation nuclei to those of other active objects, through the diagnostic diagrams by e.g. Veilleux & Osterbrock (1987), reported in Fig. 9. One sees immediately that ESO 138 G1 could be classified as a Seyfert 2 nucleus while Tol 0109–383 and IIIZw77 depart from this group of objects: it is obvious that these diagnostic diagrams are not well adapted to the case of high excitation nuclei.

The three high excitation nuclei appear to define a sequence of increasing excitation and N_e, from ESO 138 G1 to Tol 0109–383 and last to IIIZw77. There is in addition, within each of these nuclei, a density stratification. It appears that the relative importance of the high density clouds to the low density ones is increasing along the sequence from ESO 138 G1 to Tol 0109–383 and then IIIZw77. It is not possible to disentangle the excitation effects from the density effects without a complete analysis of the physical conditions within each nucleus, based upon the entire spectral information. However, the comparable strengths of [Fe X], [Fe VII] lines in all three nuclei also argue for *density effects* to be the main reason for the observed spectral differences.

It remains to be understood why IIIZw77 is devoid of low density gas clouds. As the spectral properties of IIIZw77 appear to bridge this object with radiogalaxies, we might be seeing, along the sequence ESO 138 G1→Tol 0109–383→ IIIZw77→ radiogalaxies, an increasing efficiency of matter accretion in systems with increasing total mass, from dwarf to giant galaxies.

References

Adams T.F., 1977, ApJS 33, 19

Allen D., 1979, MNRAS 186, 1P

Alloin D., Collin–Souffrin S., Joly M., Vigroux L., 1979, A&A 78, 200

Bica E., 1988, A&A 195, 76

Burstein D., Heiles C., 1984, ApJS 54, 33

de Robertis M., Osterbrock D., 1986, ApJ 301, 727

Fairall A.P., 1988, MNRAS 230, 69

Filippenko A., Halpern J., 1984, ApJ 285, 458

Fosbury R., Sansom A., 1983, MNRAS 204, 1231

Grandi S., 1978, ApJ 221, 501

Lauberts A., 1982, ESO/Uppsala Survey of the ESO (B) Atlas, ed. ESO (Garching)

Lauberts A., Valentijn E.A., 1989, The Surface Photometry Catalogue of the ESO-Uppsala Galaxies, ed. ESO (Garching)

McCall M.L., 1984, MNRAS 208, 253

Mihalszki J., Ferland G., 1983, MNRAS 205, 1279

Nussbaumer H., Storey J.P., 1978, A&A 70, 37

Nussbaumer H., Storey J.P., 1978, A&A 113, 21

Osterbrock D., 1981, ApJ 246, 696

Pagel B., Edmunds M., Blackwell D., Chun M., Smith G., 1979, MNRAS 189, 95

Pelat D., Alloin D., Fosbury R., 1981, MNRAS 195, 787

Prugniel P., Bica E., Klotz A., Alloin D., 1992, A&AS (in press)

Stasinska G., 1984, A&A 135, 341

Stasinska G., 1990, A&AS 83, 501

Smith M.G., 1975, ApJ 202, 591

Veilleux S., Osterbrock D., 1987, ApJS 63, 295